Chapter 1

Introduction

The basic structure of an atom is understood as electrons orbiting around a dense central nucleus by abstractive electromagnetic force. Modern scattering experiments discovered that the nucleus is further composed of nucleons which include protons with positive charges and electrically neutral neutrons. While the structure of nucleons has been well described by Quantum Chromodynamics (QCD), understanding the structure of the nucleus remains as one of the biggest challenges in nuclear physics due to the complicated many-body interaction between nucleons. Utilizing high energy electrons scattering on a nuclear target provides an accurate probe to detect the tiny structure of nuclei and nucleons. In this chapter, a brief review of nuclear structure examinations will be given, followed by a discussion of quasielastic (QE) electron scattering techniques.

1.1 Overview of Nuclear Structure

1.1.1 Complexity of Nuclear System

Compared with the general size of an atom, a nucleus is nearly 10^6 times smaller ($1.0fm$), within which nucleons are bound by strong interactions and form a compli-

cated many-bodies system. The general Hamiltonian describing such interactions is given by [1]:

$$H = \sum_i T(i) + \sum_{i<j} V^{(2)}(i,j) + \sum_{i<j<k} V^{(3)}(i,j,k) + \cdots, \tag{1.1}$$

where $T(i)$ is the total kinematic energies of the ith nucleon, $V^{(2)}$ and $V^{(3)}$ correspond to the two-body and three-body interactions. The corresponding time independent wave function, or the eigenstates, can be expressed as:

$$\Psi(\mathbf{r_1}, \mathbf{r_2}, \cdots, \mathbf{r_{12}}, \mathbf{r_{13}}, \cdots, \mathbf{r_{123}}, \cdots), \tag{1.2}$$

where $\mathbf{r_i}$ is the position of the ith nucleon and $\mathbf{r_{ij}}$ is the distance between the ith nucleon and jth nucleon, etc. With the knowledge of the eigenstates and eigenvalues, one can extract plentiful information from the nucleus, such as electromagnetic moments, transition rates and spectroscopic factors and etc. For a light nucleus with only few nucleons, the wave functions can be directly calculated using variational methods, such as Green Functions [2]. However, for medium and heavy nuclei, the explosion of degree of freedoms in the Hamiltonian makes it extremely difficult to obtain the solution of the many-body system.

Besides, the particular behavior of the interaction potential between nucleons also increases the complexity of the nuclear system. As shown in Fig 1.1, two nucleons experience weak interaction at moderate distance. As they are closer, the strong abstractive force, mainly caused by the tensor components of spin and isospin channels, form a deep potential well. Since nucleons are basically fermions, the hard-core interaction at short distance generates strong repulsion because of the Pauli principle which prevents the nucleus from further collapses. The Coulomb force between protons and potential three-body forces also contribute to the interactions but they are much weaker compared with the strong interactions.

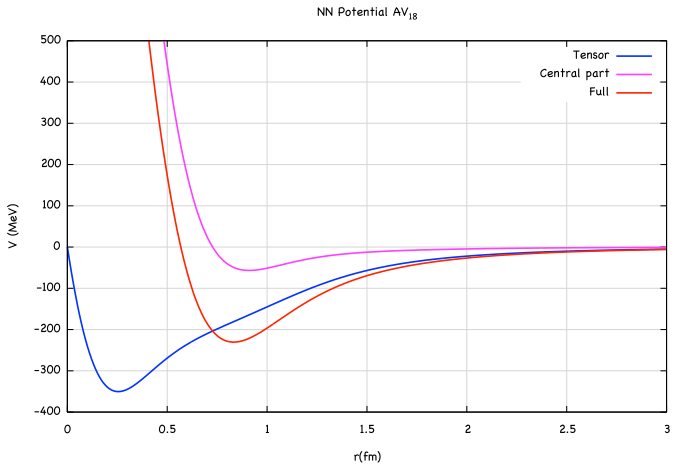

Figure 1.1: Two-nucleon potential distribution [3], where the blue line represents the tensor force which responds most of the abstractive part.

Approximation methods based on independent particle shell model (IPSM) are mostly used to study the structure of nuclei.Although there are some modern techniques, called **ab initio**, which aims to solve the many-body problems for heavy nuclei.

1.1.2 Mean Field Theory

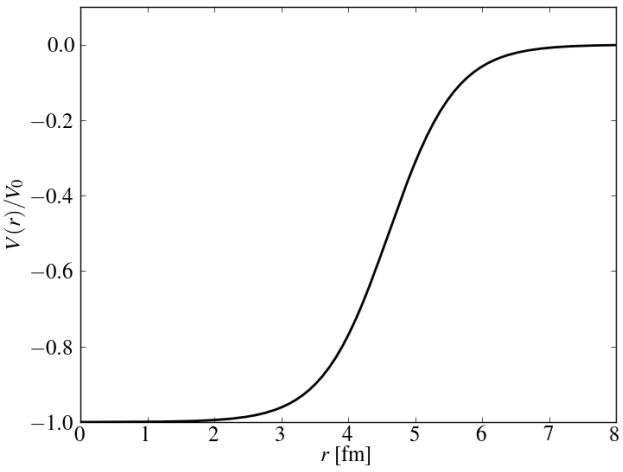

Figure 1.2: Woods-Saxon potential

Despite the complexity of the nucleus, scattering experiments reveal that nucleons behave more like independent particles in nuclear medium due to the collective effects of Pauli principle and the strong short-distant interactions with surrounding nucleons, which is usually called mean field effect. One defines the mean-free path of a nucleon inside a nucleus as $\lambda = 1/(\sigma\rho_0)$, where σ is the cross section of nucleon-nucleon interaction in the nucleus and ρ_0 is the average density of the nucleus. The bigger values of λ, the more independent the nucleons could be. Compared with the typical nucleon radius ($\sim$*1.25 fm*), the value of λ is near *1.7 fm*, which reveals that the assumption of independent particles inside the nucleus is valid. The direct consequence is that nucleons occupy different energy shells similar to the arrangement of electrons orbiting around the nucleus. The wave-function in Eq (1.2) can be obtained by solving the single particle Schrdinger equation:

$$\left(\frac{\hat{\mathbf{p}}^2}{2m} + V(\hat{\mathbf{r}}) + V_{ls}(\mathbf{r})\overrightarrow{\mathbf{L}} \cdot \overrightarrow{\mathbf{S}}\right) \mid \psi_\alpha\rangle = \varepsilon_\alpha \mid \psi_\alpha\rangle, \tag{1.3}$$

where $\mid \psi_\alpha\rangle$ and ε_α represent the eigenstate and the eigenenergy of the αth nucleon. $V(\hat{\mathbf{r}})$ is the potential of the nuclear medium, which is usually given as a combination form of the square well and the harmonic oscillator. A more realistic form of the potential is called Woods-Saxon potential [4] (Fig 1.2):

$$V(r) = \frac{V_0}{1 + exp(\frac{r-R}{a})}, \tag{1.4}$$

where $V_0 \approx -50\ MeV$ is the the depth of the potential well, $a \approx 0.5\ fm$ represents the surface thickness of the nucleus, and $R = r_0 A^{1/3}$ is the nuclear radius where A is the nuclear number and $r_0 \approx 1.25\ fm$ is the average nuclear size. Combined with the spin-orbit term, $V_{ls}(\mathbf{r})\overrightarrow{\mathbf{L}} \cdot \overrightarrow{\mathbf{S}}$, the occupation of nucleons in nuclear shell presents a remarkable pattern, called *magic numbers*, as shown in Fig 1.3. The simplified IPSM successfully predicts the ground state properties, the excitation of

nuclei at low energy, nuclear spins and parities, as well as the prediction of nuclear magic numbers. However, IPSM shows its limitation in predicting the nuclear magnet moments and highly excited energy states.

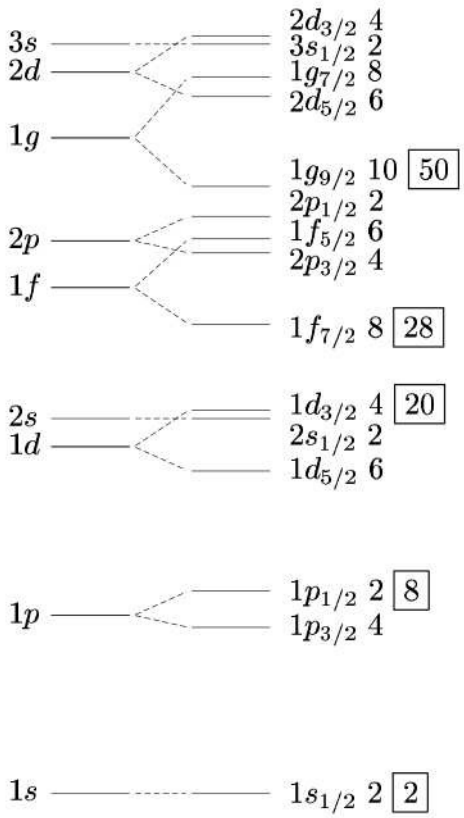

Figure 1.3: Low lying energy levels in the single particle shell model. The magic numbers are shown in the boxes.

A more sophisticated method to determine the wave function of nucleons is called **Hartree-Fock theory** (HFT) [5]. The complex N-body wave-functions are replaced by Slater determinates, which are anti-symmetrized products of N single-particle wave functions, $\sum_\alpha |\varphi_\alpha\rangle$. The choice of Slater determinates minimizes the expectation values of the Hamiltonian to force the single particles into their lowest energy states. The whole set of occupied energy levels is called the **Fermi sea**. In such a single-particle basis, the Hartree-Fock Hamiltonian is defined as [1]:

$$h_{HFT}[\rho] = t + U_{MF}[\rho] \tag{1.5}$$

where t is the kinematic energy and U_{MF} is the mean field one-body potential. $\rho = \sum_\alpha |\varphi_\alpha\rangle\langle\varphi_\alpha|$ is the one-body density matrix, where φ_α corresponds to the single-particle energy in α state. The energy of the last occupied state is called the **Fermi energy**. The minimization of the total energy leads to a simple eigenfunction [1]:

$$h_{HFT}[\rho]|\varphi_\alpha\rangle = \varepsilon_\alpha|\varphi_\alpha\rangle, \tag{1.6}$$

which is similar to Eq 1.3. However, this is a self-consistent treatment unlike directly solving the many-body Schrdinger equation, since U_{MF} depends on the one-body matrix which requires the knowledge of the single-particle states. An iteration process started with trail wave-functions is required to obtain the final solutions when the convergence is achieved.

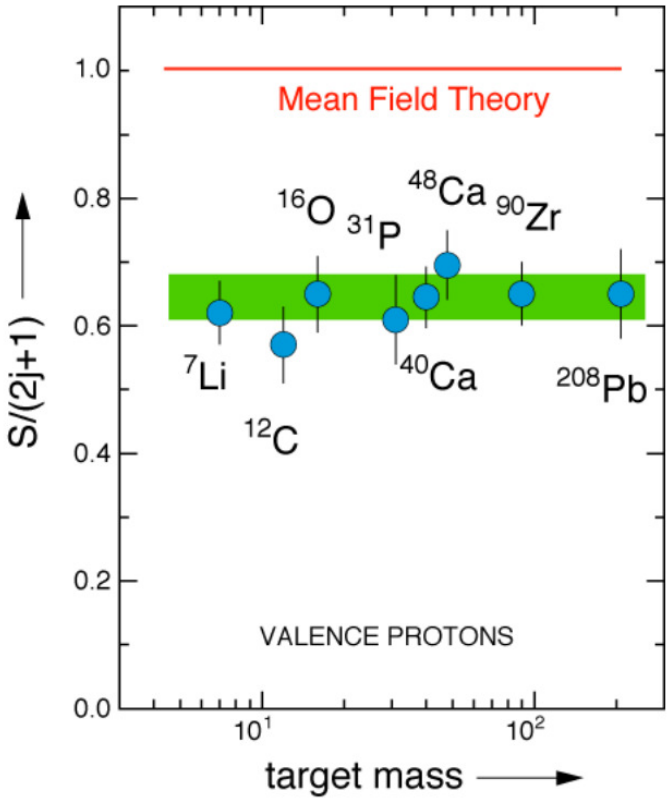

Figure 1.4: Experiment measurements of spectroscopy factors for different nuclei deviate from one, indicating the important role of correlations between nucleons.

HFT is extremely successful in the study of nuclei at low energy where IPSM is valid. Besides producing magic numbers, HFT is able to calculate the binding energy of nucleons in a wide-mass range of nuclei and to make prediction of nuclear radii. However, at a larger energy scale the interaction action brought about by nucleon-nucleon repulse force becomes significant.

A useful experimental observable, called **Spectroscopy Factor**, denotes the amplitudes of adding or removing one nucleon from the nucleus. In IPSM, assuming nucleons occupy j orbits in the nuclear shell, the cross section of removing one nucleon is then written as, $\sigma_{removing} = S \cdot \sigma_{sp}$, where σ_{sp} is the single-particle cross section, and the spectroscopy factor, S, should obey a sum role:

$$\frac{S}{(2j+1)} \equiv 1, \tag{1.7}$$

where the factor $(2j+1)$ denotes the maximum energy states of the nucleon. Several measurements [6, 7] with medium-energy proton-knock experiments in early 1970s measured the values of spectroscopy factor for heavy nuclei (Fig 1.4) which is $30\% - 40\%$ lower than one. Even advanced Hartree-Fock calculations involving long range nucleon-nucleon interaction still overestimate the nuclear strength.

1.2 Short Range Correlations

An explanation of the observed discrepancy is based on the short distance property of nucleon-nucleon strong repulsive interaction. Mean field theory restricts nucleons in their energy states below the Fermi momentum (250 MeV) when the nucleus is in its ground state. However, when two nucleons stay close due to the abstractive potential, the repulsive force prevents them from collapse but results in high relative momentum significantly exceeding the Fermi momentum. However, the total momentum of such two nucleons is still relatively small compared to excite the nucleus. The

measurement of knocking out any such highly correlated nucleons yields the nuclear strength beyond the prediction of mean field theory. Such effect is generally called short range correlations (SRCs), which will be carefully discussed in next chapter.

1.3 Quasi-elastic Scattering

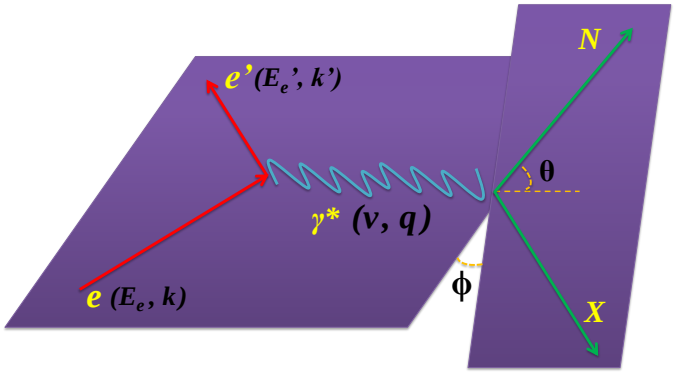

Figure 1.5: Single photon electron peaks in the sum of GC ADC spectra. Top for HRS-L and Bottom for HRS-R.

An electron with predefined initial energy and final energy, E_e and E'_e, interacts with a charged nucleus by exchanging a virtual photon with the energy transfer, $\nu = E_e - E'_e$ (Fig 1.5). By varying the amplitude of the energy transfer, one can probe the nucleus at different scales. At low energy transfer, electrons interact with the entire nucleus and the measurement of elastic cross section is generally applied in the study of nuclei and nucleons form factors [8]. As shown in Fig 1.6 [9], a process of quasi-elastic (QE) electron-nucleon scattering appears with larger energy transfer, where the virtual photon directly interacts with a nucleon, the Fermi motion of which in the nucleus results an broad distribution compared to the shape elastic peak. Nucleons are excited at even larger energy transfer and resonances start to contribute to the cross section. Electrons directly probe the quarks properties at very large energy transfer through the process of deep inelastic scattering (DIS).

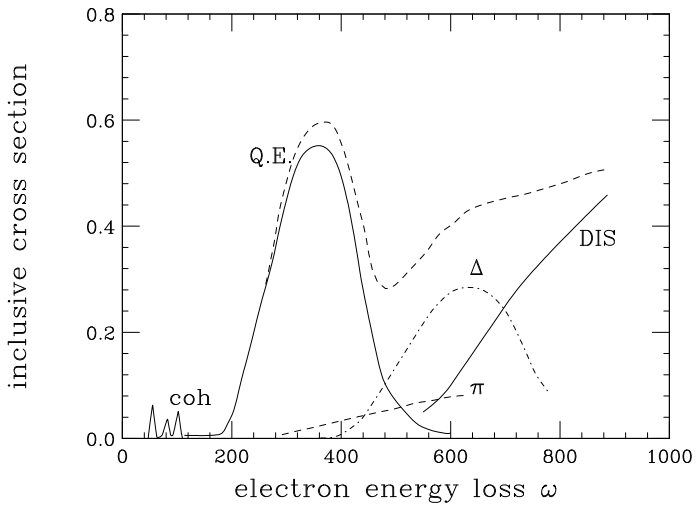

Figure 1.6: Inclusive cross section on the y-axis versus the energy loss,$\omega = \nu = E_e - E'_e$, on the x-axis.

The electromagnetic interaction through the scattering is well described by Quantum Electrodynamics (QED) and the differential cross section in the one-photon exchange approximation is given by [8]:

$$\frac{d^4\sigma}{(dE'_e d\Omega_e)(dE'_N d\Omega_N)} = \frac{2\alpha^2}{Q^4}\frac{E'_e}{E_e}|\vec{p}_N| L_{\mu\nu} W^{\mu\nu}, \tag{1.8}$$

where e and N denote the electron and the ejected particle with final energy E'_e and E'_N, respectively; E_e is the initial electron energy, $\alpha = 1/137$, and $Q_2 = 4E_e E'_e sin^4\theta/2$ is the four momentum transfer. $L_{\mu\nu}$ and $W^{\mu\nu}$ are the leptonic and nuclear response tensors [9].

A convenient parameter for identifying different processes in the scattering is the Bjorken variable, $x_{bj} = Q^2/(2m_N\nu)$, where m_N is the nucleon mass. The original definition of x_{bj} is the momentum fraction of the quark constituents from the nucleon during the scattering. In electron-nucleon scattering, the elastic peak locates at $x_{bj} = 1$, while for inelastic process, $0 < x_{bj} < 1$. In electron-nucleus scattering, x_{bj} extends to the region of $0 < x_{bj} < M_A/m_N$, $x_{bj} = 1$ is now the location of the quasi-elastic peak, and the elastic peak moves to $x_{bj} = M_A/m_N$. For convenience, m_N is usually

replaced by the proton mass during the experimental data analysis, as used in the rest of this thesis:

$$x_{bj} = Q^2/(2m_p\nu). \tag{1.9}$$

During the quasi-elastic scattering, an electron knocks a nucleon out from the nucleus (Fig 1.6), which provides a opportunity to study the property of nuclear structure. In the picture of plane-wave impulse approximation (PWIA), the exclusive electron scattering cross section can be written as a sum of the exclusive cross section over the whole phase space for the knock-out nucleon [10]:

$$\frac{d^5\sigma}{dE'_e d\Omega_e d^3\vec{p'}} = \sum_{nucleons} \sigma_{eN} \cdot S'_N(E_0, \mathbf{p_0}), \tag{1.10}$$

where $S'_N(E_0, \mathbf{p_0})$ is the probability of removing a nucleon with initial energy E_0, or called the nuclear spectral function, and momentum $\mathbf{p_0}$ from the target nucleus [9], and σ_{eN} is the electron-nucleus cross section.

1.3.1 Inclusive Cross Section

The inclusive electron scattering cross section is measured by only detecting the scattered electrons, while the final state of the target remains unknown. To obtain the inclusive cross section from Eq (1.10), one separates the contributions from protons and neutrons, and integrals over the final states of the nucleons:

$$\frac{d^3\sigma}{dE'd\Omega} = \int (Z\sigma_{ep}S'_p(E_0, \mathbf{p_0}) + N\sigma_{en}S'_n(E_0, \mathbf{p_0}))d^3\mathbf{p'}, \tag{1.11}$$

where the subscripts in $dE'_e d\Omega_e$ have been omitted since only electrons are measured.

For unpolarized scattering, the spectral function is spherically symmetric, and if the difference in the spectral function between protons and neutrons is ignored, the more general form $S'(E_0, p_0)$ can be factored out from the equation. Since $\mathbf{p'} = \mathbf{p_0} + \mathbf{q}$,

where $\mathbf{q}$ is fixed during one kinematic setting, one can replace $d^3\mathbf{p'}$ by $d^3\mathbf{p_0}$. In the spherical coordinate, $d^3\mathbf{p_0} = p_0^2 dp_0 d(cos\theta)d\phi$, and the cross section becomes:

$$\frac{d^3\sigma}{dE'd\Omega} = 2\pi \int \tilde{\sigma}_0 \cdot S'(E_0, p_0) \cdot p_0^2 dp_0 d(cos\theta) \tag{1.12}$$

where

$$\tilde{\sigma}_0 = \frac{1}{2\pi} \int_0^{2\pi} (Z\sigma_{ep} + N\sigma_{en})\, d\phi. \tag{1.13}$$

By considering the energy and momentum conservations,

$$(M_A - E_0)^2 = M_{A-1}^{*2} + p_0^2, \quad M_A + \nu = \sqrt{M^2 + (\mathbf{p_0}^2 + \mathbf{q}^2)} + \sqrt{M_{A-1}^{*2} + \mathbf{p_0^2}}, \tag{1.14}$$

where M, and M_A are the mass of the ejected nucleon and the target nucleus, respectively. M_{A-1}^* is the mass of the recoiling $(A-1)$ system, where the superscript * means it could be in its excited state. Eq 1.12 becomes [10]:

$$\frac{d^3\sigma}{dE'd\Omega} = 2\pi \int \tilde{\sigma}_0 \cdot \frac{E_N}{|\mathbf{p_0}||\mathbf{q}|} \cdot S'(E_0, p_0) \cdot p_0^2 dp_0 dE_0 \tag{1.15}$$

One can define the separation energy, $E_s \equiv M_{A-1}^* + M - M_A$. Then through the Jacobian transformation, the spectral function becomes $S(E_s, p_0) \equiv -B_{Jacobian} \cdot S'(E_0, p_0)$, where $B_{Jacobian}$ is a transformation factor absorbed into the new definition. One can define $\tilde{\sigma} = \tilde{\sigma_0} \cdot E_N/|\mathbf{q}|$, and rewrite the cross section as:

$$\frac{d^3\sigma}{dE'd\Omega} = 2\pi \int_{E_s^{min}}^{E_s^{max}} \int_{p_0^{min}}^{p_0^{max}} \tilde{\sigma} \cdot S(E_s, p_0) \cdot p_0 dp_0 dE_s, \tag{1.16}$$

where p_0^{min} and p_0^{max} are the solution of Eq (1.14) when $\mathbf{p_0}$ and $\mathbf{q}$ are parallel [10]. E_s^{max} is the maximum separation energy when the struck nucleon is at rest, while E_s^{min} corresponds to the minimum separation energy when the recoil nucleus is in its ground state.

1.3.2 Spectral Function and Momentum Distribution

In the shell model, nucleons move as independent particles in a mean field and the spectral function can be written as [9]:

$$S_{MF}(E_0, \mathbf{p_0}) = \sum_{n \in F} |\phi(\mathbf{p_0})|^2 \delta(E_0 - E_n), \tag{1.17}$$

where $\phi_{\mathbf{p_0}}$ is the wave function in the momentum space for a nucleon with the eigenstate E_n, and the sum is over all occupied states belong to the Fermi sea $\boldsymbol{F}$.

The validity of the mean field theory can be examined by studying the distribution of the spectral function as a function of E_0 through electron-nucleon and hadron-nucleon knock-out experiments. The peaks in the distribution correspond to knocking out nucleons from orbits defined by shell model and any discrepancy indicates the effect of nucleon-nucleon interaction. The full spectral function includes an extra term to take into account the effect [9]:

$$S(E_0, \mathbf{p_0}) = S_{MF}(E_0, \mathbf{p_0}) + S_{Corr}(E_0, \mathbf{p_0}), \tag{1.18}$$

The correlation term provides an important test of advanced interacting shell model calculations thought direct experimental measurements base on the normalization requirement:

$$\int S(E_0, \mathbf{p_0}) d^3\mathbf{p_0} dE_s = 1. \tag{1.19}$$

The integral of the spectral function over the separation energy leads to the momentum distribution:

$$n_{p_0} = \int_{E_s^{min}}^{\infty} S(E_s, p_0) dE_s. \tag{1.20}$$

The momentum distribution is a sensitive probe to examine the effect of the nuclear medium and nucleon-nucleon interactions. At the momentum above the Fermi momentum, k_F, the mean field effect vanish and strong short range correlations of the

nucleons emerge.

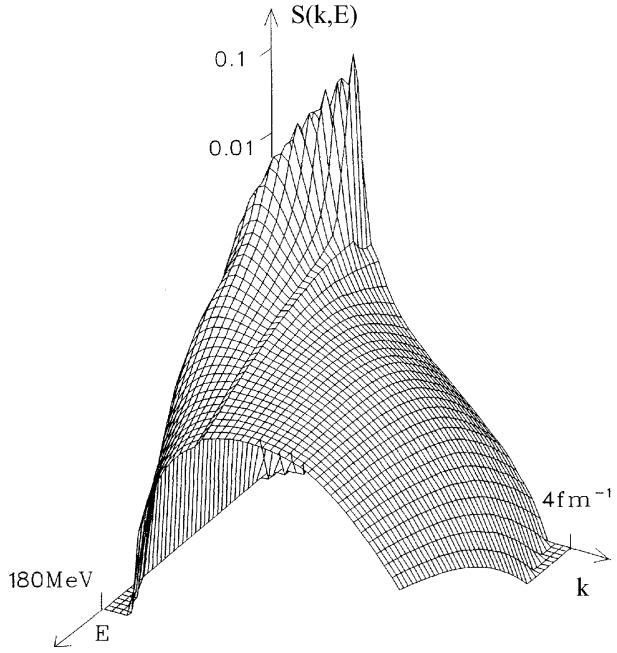

Figure 1.7: Spectral Function versus separation energy E_s and transfer momentum p_0.

Shown in Fig 1.7, the upper limits of the two integrals in Eq (1.16) can be extended to infinity because the spectral function decreases rapidly by orders of magnitude toward E_s^{max} and p_0^{max}. Meanwhile, $\tilde{\sigma}$ changes very slow as a function of E_s and p_0 so can be factored out from the integral and evaluated at the maximum value of the spectral function at $E_s = E_s^0$. Hence Eq (1.16) can be rewritten as:

$$\frac{d^3\sigma}{dE'd\Omega} = 2\pi\bar{\sigma}\int_{E_s^{min}}^{\infty}\int_{p_0^{min}}^{\infty} S(E_s, p_0)\cdot p_0 dp_0 dE_s, \tag{1.21}$$

where $\bar{\sigma} \propto \tilde{\sigma}(E_s^0, p_0^{min})$ [11]. The model of $\bar{\sigma}$ is usually taken from the prescription by De Forest [12], shown as [10]:

$$\bar{\sigma} = \frac{1}{Z\sigma_p + N\sigma_n}\frac{|\mathbf{q}|}{\sqrt{M^2 + (y+\mathbf{q})^2}}. \tag{1.22}$$

1.3.3 y-Scaling

The spectral function directly links to the momentum distribution which represents the nucleon response in the nucleus, but it is not an experimental observable. Instead, one can examine the scaling behavior [13] of inclusive quasielastic scattering cross section to study the substructure of the nucleus. The scaling function can be defined as [14, 15]:

$$F(y, \mathbf{q}) = 2\pi \int_{E_s^{min}}^{\infty} \int_{|y|}^{\infty} S(E_s, p_0) \cdot p_0 dp_0 dE_s. \tag{1.23}$$

where the new variable, y, is defined as the minimum values of momentum in Eq (1.14), $p_0^{min} = |y|$, when the $A-1$ system is in its ground state:

$$M_A + \nu = \sqrt{M^2 + \mathbf{q^2} + y^2 + 2y|\mathbf{q}|} + \sqrt{M_{A-1}^2 + y^2}. \tag{1.24}$$

If only the nucleonic degrees of freedom are considered, the scaling function becomes independent of $\mathbf{q}$ at large momentum transfer [15]. Hence, $F(y, \mathbf{q}) \equiv F(y)$. From Eq (1.21), the scaling function can be extracted from electron-nucleon scattering cross section for an off-shell nucleon:

$$F(y) = \frac{d^3\sigma}{dE' d\Omega} \frac{1}{Z\sigma_p + N\sigma_n} \frac{|\mathbf{q}|}{\sqrt{M^2 + (y + \mathbf{q})^2}}. \tag{1.25}$$

Due to the Fermi motion, the broad quasielastic peak of the inclusive cross section is mixed with the tails of resonance and DIS components, as shown in Fig 1.6. To extract $F(y)$ from the experimental cross section, one needs to utilize a cross section model to remove the contribution from DIS region, $\sigma_{QE} = \sigma_{Exp} - \sigma_{DIS}^{model}$ (See Appendix B).

From Eq (1.20), $F(y)$ can also be rewritten as:

$$F(y) = 2\pi \int_{|y|}^{\infty} n(p_0) \cdot p_0 dp_0. \tag{1.26}$$

Hence the momentum distribution can be extracted experimentally by measuring the $F(y)$ distribution [9]:

$$n(p_0) = \frac{-1}{2\pi p_0}\frac{dF(y)}{dy}. \tag{1.27}$$

The scaling of $F(y)$ is valid only at moderate large Q^2. In Eq (1.23), the integration limits have been extended to infinity and the error raised from this approximation must be small. An assumption has been made in Eq (1.26) that the momentum distribution is independent of E_s, which requires the small effect of the missing energy in the kinematic region.

1.3.4 Final State Interaction

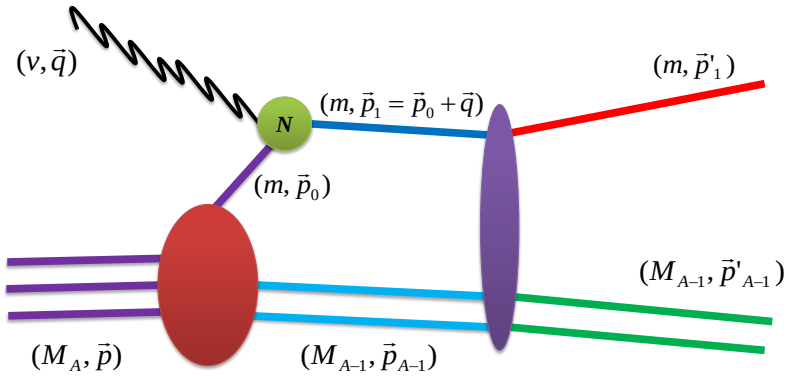

Figure 1.8: General diagram of final state interaction. The struck nucleon is re-scattered by the $A-1$ system and its final momentum is modified.

Final State Interaction (FSI) is the effect of the struck nucleon being re-scattered by the $A-1$ recoil system. In PWIA, the nucleons in the nucleus are treated as individual constituents and the space resolution of the electron probe is approximately $1/q$. Hence, in the inclusive cross section measurement at large Q^2, FSI is negligibly small, based on the fact that the interaction time between the virtual photon and the

struck nucleon is significant smaller than the one between the struck nucleon and the recoil system.

However, comparison between the theoretical calculation and experimental results [16, 17] shows the violations of y-scaling for heavy target which indicates FSI still plays a significant role in the scattering process even at large Q^2. (MORE discussion)

Chapter 2

Short Range Correlations in Nuclei

Despite the great success in description of the nuclear structure as individual nucleons being in their low-lying energy shell within the Fermi momentum, k_F, the mean field theory provides limited ability to study the short range properties of nucleon-nucleon (NN) interaction and fails to investigate the structure of nuclear matter beyond the saturation density. The observed nuclear strength is significantly lower than the expectation value in shell model. **Short Range Correlations (SRCs)** provide an successful explanation of such discrepancy by examining the high momentum component of the nucleon momentum distribution at $k > k_F$. The abstractive and repulsive potentials between nucleons at short distance ($\sim$ 1.0 fm) excite the nucleons from their single shell and cause the significant increase of strength to the nuclear spectral function.

During the early study of nuclear structre though scattering experiments, SRCs were not considered as an important feature due to the limitation of high energy processes. The existence of high energy and high luminosity electron accelerators, i.e., SLAC and JLab, provide a good opportunity to directly probe the nucleon properties beyond their low-lying shells and to study the high momentum component of nuclear wave function where SRCs are considered to be dominant. Early experiments in

SLAC conformed the evidence of SRCs and recent experiments in JLab extended the study to map out the strength of SRCs in different nuclei and examined the isospin effect in SRCs. In this chapter, the new development of theoretical understandings of nuclear properties will be carefully explained and experimental techniques to explore SRCs will be briefly reviewed.

2.1 The Features of SRCs

To understand why the mean field theory fails to predict the nuclear strength and how SRCs attribute to the explanation of the missing nuclear strength, one needs to examine the modern nucleon momentum distributions which directly relate to the nucleon properties in the nucleus. While the prediction of mean field theory gives a rapid failing off curve at momenta approaching k_F, shown in Fig 2.1, experimental results [18] present the momentum tail with much slow falloff at $k > k_F$ which is similar for all nuclei from Deuterium to nuclear matter. Such a universal feature strongly argues again the mean field calculation, but can be easily understood if the high momentum tails are generated by the short-range part of NN interactions, i.e., SRCs.

From Fig 1.1, nucleons interact at very short distance via the abstractive potential which is mainly contributed by the tensor force, but their strong repulsive hard-cores prevents them to further collapse. Such dramatic processes end up with in a correlated configuration with large relative momenta which exits the shell energies. The excitation of nucleons in this configuration significantly increases the nuclear strength at $k > k_F$ which is underestimated by the mean field theory. However, the excitations are compared to the mean field ground state of the nucleus but not related to any real excited statues of the nucleus. The small total momentum of the correlation nucleons contributes to the true nuclear ground statues.

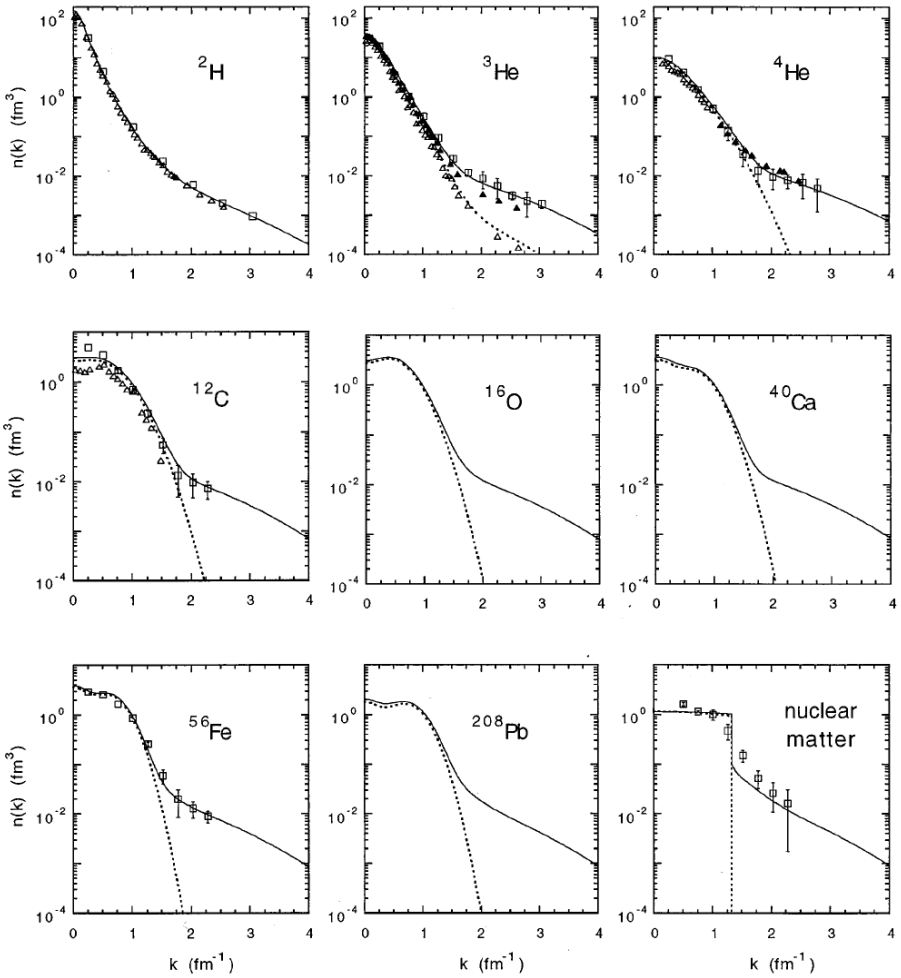

Figure 2.1: Nucleon momentum distribution for various nuclei [18], where dotted lines are from a mean field calculation, solid lines are from calculations involving SRCs. Dots are from experimental data.

In the picture of SRCs, the asymptotic form of momentum distribution can be broke down into several regions. At $k \leq k_F$, the potential is mainly contributed by the mean field potential which gives degenerate Fermi systems for different nuclei. At the momentum range $300 < k < 600\ MeV/c$, the contribution of the mean field effect vanishes and the effect of two-nucleon short range correlation (2N-SRC) becomes dominant. In 2N-SRC, two nucleons carry high relative momenta with back-to-back direction, hence their total momentum is negligible. Due to the fact that the NN abstraction is dominated by the tensor components which yields iso-singlet pairs

$(np)_{I=0}$, one expects to see the high momentum tails of heavy nuclei to be identical to the one of Deuteron, as shown in Fig 2.1. The configuration of 2N-SRC breaks down at much higher momentum limit ($600 \leq k \leq 800\ MeV/c$) where the isospin-independent repulsive core dominates, and the inclusion of three-nucleon short range correlation (3N-SRC) should be manifested [19]. However, 3N-SRC is not as significant as 2N-SRC since it is the result of the interaction of two-body interaction. At extremely high k limit where the nucleon kinematic energy is comparable with the excitation energy of nucleons, non-nucleonic degree-of-freedom may be needed to be considered [19].

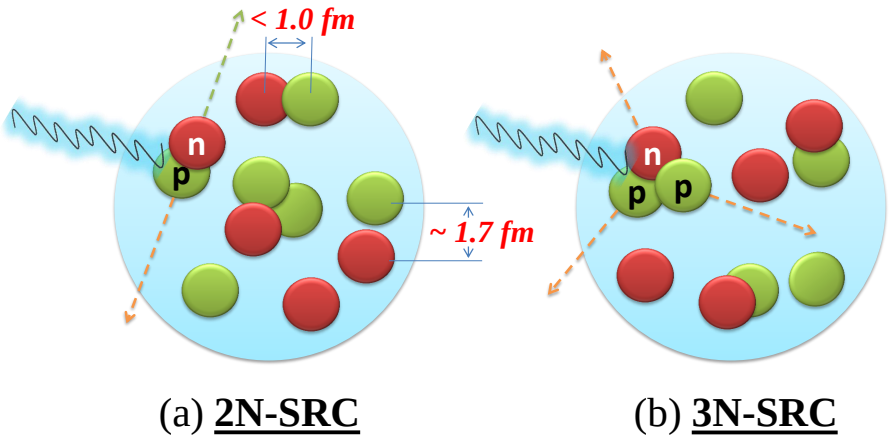

Figure 2.2: Diagram of 2N- and 3N-SRC, where nucleons are weakly interacting at normal distance ($\sim 1.7\ fm$) while the wave-functions of nucleons in 2N- or 3N-SRC are strongly overlapped. On the left diagram the virtual phone breaks up the 2N-SRC pair in back-to-back ejection, and on the right diagram the break-up of 3N-SRC configuration results in correlated nucleon ejecting in different direction so their total momentum remains at zero.

Based on the discussion above, and assuming that the potential decreases at large k, like $V(k) \sim \frac{1}{k^n}$, the nuclear wave-function of the nucleon at large k is given in the 2N-SRC form [20]:

$$\psi_A(k_1, k_2, k_3, ..., k_A) \sim \frac{V_{NN}(k)}{k} \cdot f(k_3, ..., k_A), \tag{2.1}$$

where $k = k_1 = -k_2$ (Fig 2.2) and $f(k_3, ..., k_A)$ is a smooth function of the momenta of

spectator nucleons in the recoil system. And the momentum distribution is dominated by the contribution from 2N-SRC:

$$n(k) \sim \left(\frac{V_{NN}(k)}{k^2} \right)^2 . \tag{2.2}$$

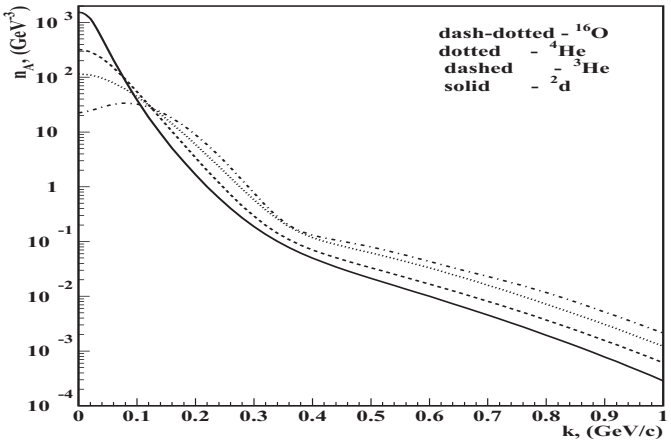

Figure 2.3: Comparing momentum distribution for different nuclei [20]

The results of this equation are compared among ^2H, ^3He, ^4He, and ^{16}O, as shown in Fig 2.3, where the similarities of the momentum distribution for different nuclei are clearly reproduced. Other calculation of the momentum distribution based on relativistic nuclear theory also conform the dominance of 2N-SRC for the high momentum tail [20, 21].

2.1.1 Two-Nucleon Correlations

The dominance of 2N-SRC in the nucleus should yield an momentum distribution proportional to the one of Deuterium at $k > k_F$:

$$n_A(k) = a_2(A, Z) \cdot n_D(k), \qquad for \quad k > k_F, \tag{2.3}$$

where $n_D(k)$ denotes the momentum distribution of Deuterium and $a_2(A, Z)$ relates to the probability of finding such two-nucleon configuration in the nucleus with nuclear number A and proton number Z. One can study the scaling of a_2 as the function of k, by taking ratio of momentum distribution of different nuclei to Deuterium,$n_A(k)/n_D(k)$, as shown in Fig 2.4. A better quantity used for the analysis is defined as:

$$n(k_z) = \int n(k) d^2 k_\perp, \tag{2.4}$$

of which the distribution is denoted as lines in Fig 2.4 and shows better scaling behaviour.

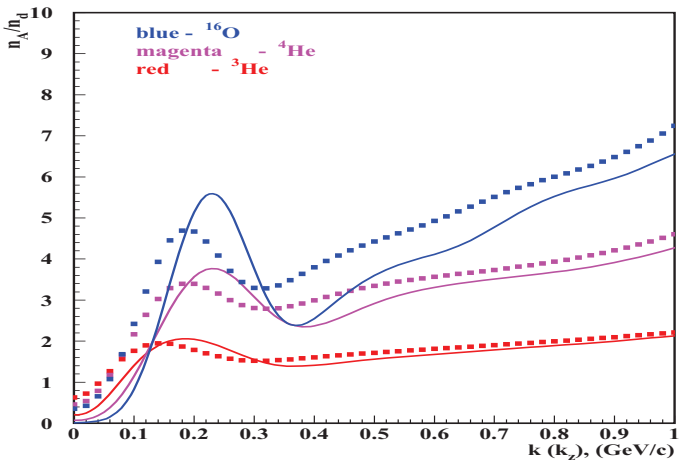

Figure 2.4: Momentum distribution ratio of nuclei w.r.t Deuterium [20], where curves represent the ratio $n_(A)(k)/n_D(k)$ and points denote the distribution of $n(k_z)$ ratio.

The momentum distribution can be reconstructed from the ground state wave-function but it is not an experimental observable. Instead, one studies the spectral function in SRCs since it directly relates to the cross section of physical processes (Eq 1.10). Similar to the definition in the shell model (Eq (1.17)), in SRCs, one can define the spectral function as [20]:

$$S_A(E_R, p_i) = | < \phi_{A-1} | \delta(-p_i^2/(2m_{A-1}) + E_R - E_m) a(k) | \psi_A > |^2, \tag{2.5}$$

which represents a product of the probability of finding a nucleon in the nucleus with initial momentum p_i, and the probability of the residual system carrying recoil energy E_R after the removal of this nucleon. *a(k)* denotes an operator to remove a nucleon from the nucleus A, E_m depends on A and represents the excitation energy of the $A-1$ system at rest, and $-p_i^2/(2m_{A-1})$ is the kinetic energy of the center of mass.

When a nucleon in the 2N-SRC configuration is instantly removed by a high energy probe, its paired nucleon with an equal momentum is rejected in the opposite direction, while the $A-2$ residual nucleus remains unperturbed ($E_m \sim 0$). From Eq (2.5) the average recoil energy of the $A-1$ system can be approximately given as:

$$< E_R >_{2N-SRC} \sim \frac{p_i^2}{2m_N}. \tag{2.6}$$

Observation of the correlation between the spectral function and E_R enables one to examine the contribution of SRCs but however, it is not uniquely sensitive to SRCs. Indeed, any processes that involving NN interaction, such as meson exchange currents,yields the same result in Eq (2.6). One can check the dominance of the SRCs by applying additional kinematic conditions to suppress long range NN interactions, which will be discussed in next section.

2.1.2 Three-Nucleon Correlations

Similar to the Deuterium-like configuration of the 2N-SRC pair, The momentum distribution of a nucleon in a 3N-SRC configuration should be identical to the case in ^3He:

$$n_A(k) = a_3(A,Z) \cdot n_{^3He}(k), \qquad for \quad k > 800 \quad MeV/c, \tag{2.7}$$

where similarly, $n_{^3He}(k)$ is the momentum distribution of ^3He and $a_3(A,Z)$ is the probability of finding three-nucleon configuration in the nucleus A. The similar scaling behaviour of 3N-SRC is shown in Fig 2.5.

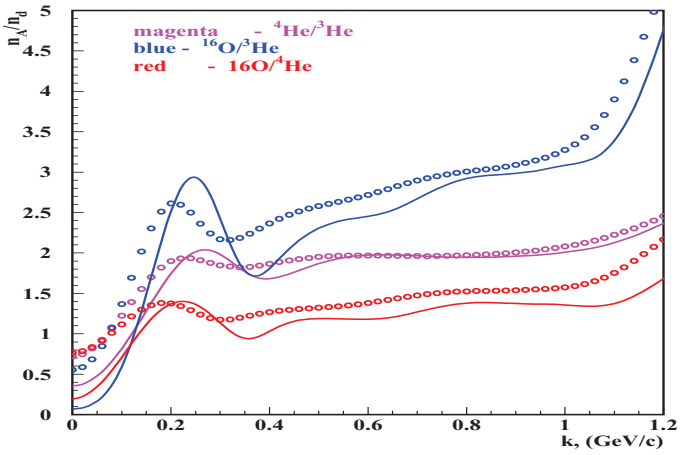

Figure 2.5: Momentum distribution ratio of nuclei w.r.t ${}^3He$ and ${}^4He$ [20], where curves represent the ratio $n_A(k)/n_{3(4)He}(k)$ and points denote the distribution of $n(k_z)$ ratio.

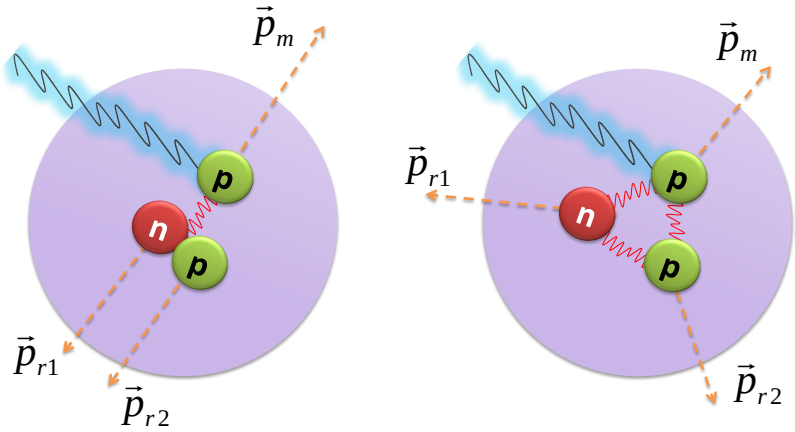

(a) **3N-SRC-I** (b) **3N-SRC-II**

Figure 2.6: Two types of 3N-SRC configuration [20].

However, the configuration of 3N-SRC is more complicated compared with the simple back-to-back picture of 2N-SRC. In general, there are two types of 3N-SRC, as shown in Fig 2.6. The first type, namely 3N-SRC-I, is the situation of two nucleons share the initial momentum which is equal to the struck nucleons but in the opposite direction, a configuration similar to 2N-SRC but involving three nucleons. The effect of 3N-SRC-I typically dominates at $p_i \geq 600 MeV/c$ with the average recoil energy of

the $A-2$ residual system:

$$< E_R >_{3N-SRC-I} \sim \frac{p_i^2}{4m_N}. \tag{2.8}$$

which is approximately equal to one half of the recoil energy in 2N-SRC. This configuration gives the major contribution in the kinematic region of 3N-SRC.

Meanwhile, the second type, 3N-SRC-II, refers to the configuration of three nucleon carrying momenta all exceeding Fermi momentum and in three different direction, and the average recoil energy of the residual system in this configuration is:

$$< E_R >_{3N-SRC-II} \sim \frac{p_i^2}{m_N}, \tag{2.9}$$

which is larger than the average recoil energy of 3N-SRC-I, indicating the probability of 3N-SRC-II is more rare than the one of 3N-SRC-I, although the former one is easier to be observed experimentally.

Eq (2.6), Eq (2.8) and Eq (2.9) reveal that the average recoil energy of 2N-SRC is in between the two average recoil energies of 3N-SRC, and for 2N-SRC the distribution of E_R as a function of p_i is very broad, so its capability of identifying contributions from 2N-SRC and 3N-SRC to the spectral function is limited. A new kinematic quantities is desired to separate these two processes, which is introduced next.

2.1.3 Relativistic Approach

The high energy process of knocking out short range correlated nucleons with very high momenta make one more naturally to apply the study of SRCs in the relativistic regime. The relativistic projectile moving along the z-direction probe the light-cone (LC) wave-function of the nucleus, $\psi_A(\alpha_1, k_{1,t}, ..., \alpha_i, k_{i,t}, ..., \alpha_A, k_{A,t})$, where the LC

variable is defined as [20]:

$$\alpha_i = A\left(\frac{E_i - p_{i,z}}{E_A - p_{A,z}}\right) = A\left(\frac{E_i^{lab} - p_{i,z}^{lab}}{M_A}\right), \tag{2.10}$$

where $(E_i - p_{i,z})$ and $(E_A - p_{A,z})$ are the initial energy and longitudinal momentum of constituent nucleons and the target nucleus, A, respectively. α_i is invariant under Lorentz boosts in the z-direction. In the rest frame of the nucleus, $E_A - p_{A,z} = M_A$, where M_A is the nuclear mass.

Similar to the definition of x_{bj} in inelastic scattering (Eq 1.9), α_i denotes the LC fractions of the nucleus momentum carried by the nucleon, hence $\sum_i^A \alpha_i = A$. While $\alpha_i \leq 1$ limits the momentum fraction of the nucleon carried by the quark, to have $\alpha_i > 1$ requires at lease two nucleons to involve in the scattering. Furthermore, three nucleons are required to share their momentum to have $\alpha_i > 2$. Consequently, α_i becomes an idea variable to distinguish the processes of 2N-SRC, 3N-SRC and so on. Considering the energy and momentum conservation law for the nucleon knock-out with a virtual photon from the nucleus, one can rewrite the LC variable as [19]:

$$\alpha_i = x_{bj}\left(1 + \frac{2p_{i,z}}{\nu + |\mathbf{q}|}\right) + \frac{W_N^2 - m_i^2}{2m_i\nu}, \tag{2.11}$$

where ν and $\mathbf{q}$ is the energy and momentum transfer of the virtual photon, respectively, and $W_N^2 = (\mathbf{p_i} + \mathbf{q})^2$. For quasi-elastic process, $W_N \simeq m_i$ yields a simple connection between α_i and x_{bj}. At sufficiently large Q^2, α_i is usually replaced by x_{bj}:

$$\alpha_i \to x_{bj}, \quad for \quad Q_2 \to \infty. \tag{2.12}$$

However, two variables have distinct difference for Q^2 values at few GeV^2 range. One needs to examine the different scaling of SRCs as a function of x_{bj} and α_i at the region of low Q^2 values.

2.1.4 Isospin Effect

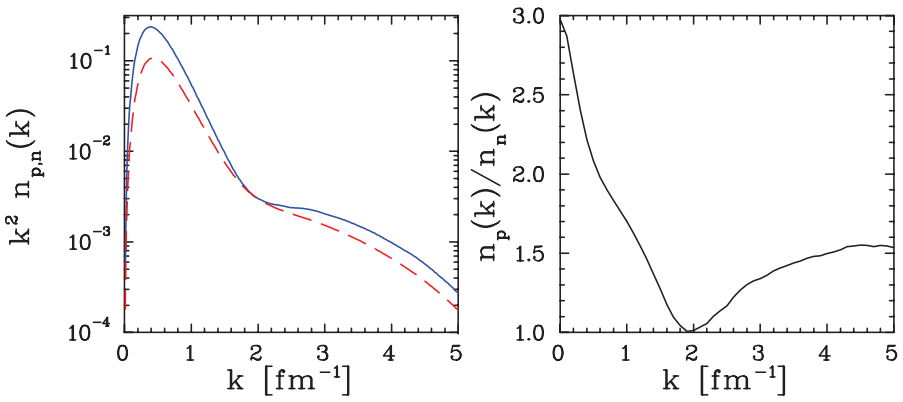

Figure 2.7: Left: Momentum distribution for proton (solid) and neutron (dashed) in ^3He; Right: Ratio of proton to neutron momentum distribution.

Early analysis assumed the isospin-independence of SRCs, which means that the ratio of neutrons to protons in SRCs is equal to the N/Z ratio of the nucleus. However, numerical studies [22] and experimental evidences [23] reveal that the tensor interaction dominates the attractive potential of 2N-SRC. Consequentially, one expects that 2N-SRC pairs should be mainly in iso-singlet ($np, T = 0$) states. The iso-triplet (pp,np and nn,$T = 1$) pairs can be close together without interaction strongly until their repulsive forces become strong [19].

Fig 2.7 shows a calculation of the momentum distribution for protons and neutrons and their ratio in $^3H3$ [24]. In the assumption of isospin-independence, the momentum ratio of protons to neutrons should be equal to two, but if the SRCs are isospin-dependent, the ratio becomes one when SRCs dominate at $k > k_F$. The left plot gives the value of the ratio at $k > k_F$ roughly equal to 1.5, which suggests that the isospin

effect largely deviates from the assumption of isospin independence. The reason why $np_{T=0}$ configuration does not totally dominates is that the $T = 1$ channels are not completely suppressed, especially at very large momentum, where the configuration of 3N-SRC is more complicated. Another calculation [25] extended the study to other nuclei provides the similar results. Shown in Fig 2.8, the momentum distribution of np pairs is much more significant than one of the pp pairs at $300 < k < 600\ MeV/c$.

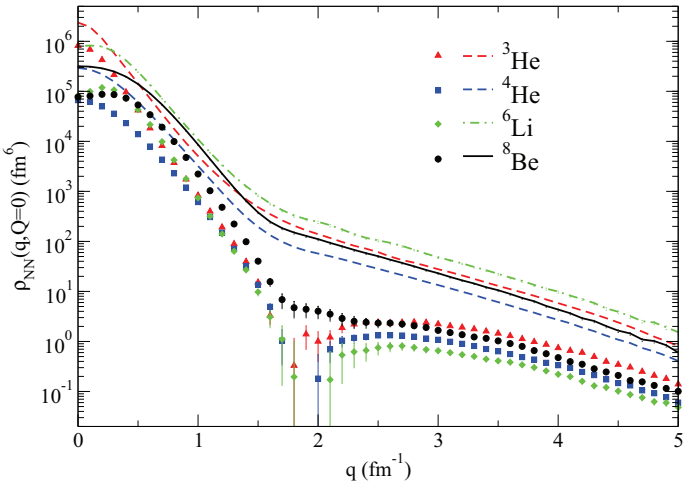

Figure 2.8: Isospin effect in momentum distribution, where lines represents the momentum distribution in np and dots represents the momentum distribution in pp. The dip in the pp dots is due to the nucleon-nucleon tensor interaction [25].

The isospin effect in 2N-SRC can be studied by triple-coincidence experiments, which not only measures electrons and the struck protons originally in a 2N-SRC configuration but also simultaneously counts the number of protons and nucleons in the opposite direction with equal momentum. Inclusive cross sections is also sensitive to such effect. One can examine the isospin-dependence by measuring the cross section ratio of two isotopes at SRCs region, such as $^{48}Ca/^{40}Ca0$ [26] and $^3He/^3H$ [27], which will be discussed in next section.

2.2 Probing SRCs using Electron Scattering

To isolate the high momentum nucleons and perform clean measurements of SRCs in nuclei, one needs to carefully selecting the proper kinematics settings to suppress other competing processes during scattering. By identifying the process of high energy probes instantly removing the nucleon from SRCs, one is able to extract reliable information on the spectral function and momentum distribution from the measured observables. Meanwhile, it is essential to distinguish the struck and the spectator nucleons from SRCs to understand the dynamical mechanism of SRCs in the nuclear ground state wave-function, for instance, the center-of-mass motion of nucleons in SRCs in the nuclear medium. As discussed in previous section, contributions from 2N-SRC and 3N-SRC in the spectral function can not be well separated by examining the recoil energy of the residual system. A specific reaction and a kinematic variable are required to study two processes separately.

A nucleus is a complicated system and the struck nucleon experiences different interactions both in its initial state and final state. Long range two-step interactions, such as meson exchange current (MECs) and intermediate state resonances, dominate the momentum distribution and their extension to higher k will significantly alter the picture of SRCs. The major problem in the experimental study of SRCs is the final state interaction (FSI) effects, where the information of the struck nucleon's momentum and energy can be largely distorted during the re-scattering processes with other spectators in the residual system. Fully understanding the role of FIS during the study of SRCs in electron-nucleon scattering from the nucleus is crucial.

2.2.1 Kinematics Conditions

Although there are different kinds of reactions for probing SRCs, there share the common kinematic conditions to provide a clean study. Overall, the desire to instantly

remove the nucleon from the SRCs can be achieved by requiring sufficiently large energy and momentum transfer scales which significantly exceed the excitation scale of the nucleus [20, 21]

$$\nu >> V_{NN}, \qquad |\mathbf{q}| >> m_N/c, \tag{2.13}$$

where V_{NN} is the characteristic potential of the NN interaction and m_N is the nucleon mass. An reaction of removing a nucleon from the nucleus under this condition allows the residual system to remain intact, where the spectral function will directly reflect the properties of SRCs [19].

The contribution of long range interactions, such as MECs, is suppressed by a factor of Q^{-4} with respect to the production of SRCs, and can be generally suppressed by requiring [28]:

$$Q^2 > 1.0\ GeV^2 >> m^2_{meson}. \tag{2.14}$$

In this condition, intermediate state resonances, such as the isobars current (IC), still have sizeable contribution. For example, for $1\ GeV^2 < Q^2 < 4\ GeV^2$, $\gamma N \to \Delta$ transition is comparable with $\gamma N \to N$. Those resonance states are generally within the region of $0 < x_{bj} < 1$, and their contributions can be suppressed by working at the region above the quasi-elastic scattering:

$$x_{bj} > 1. \tag{2.15}$$

Fig 2.9 demonstrates that the combination of kinematic conditions (Eq (2.14) and Eq (2.15)) results in probing the nucleon from the 2N-SRC with the minimum momentum above the Fermi momentum ($p_{min} > k_F$), where there is almost no contribution from the mean field part of the nucleon momentum distribution. When Q^2 value is not sufficiently large ($\sim 0.5\ GeV^2$), the 2N-SRC production is almost merged by other processes even at very higher x_{bj} (~ 1.8). At very high Q^2 ($\sim 10\ GeV^2$), the minimum momentum requirement of the struck nucleon easily archives at relatively

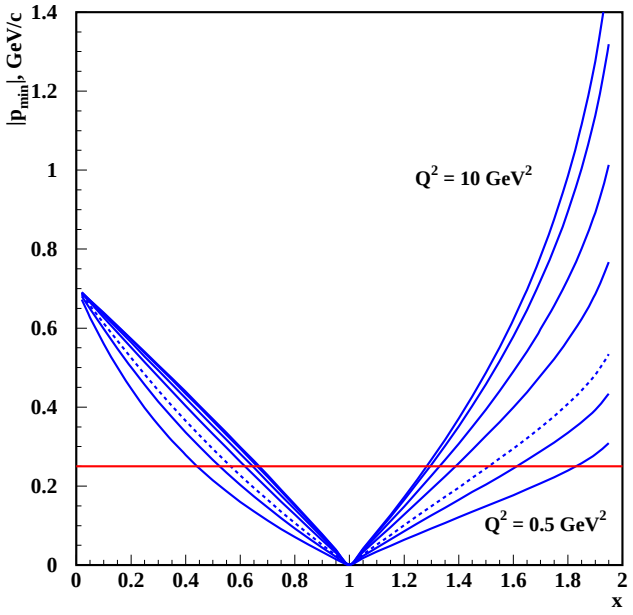

Figure 2.9: Minimum momentum of the struck nucleon as function of x_{bj} and Q^2 for Deuterium, where the red line sets the value of the Fermi momentum (k_F).

low x_{bj} (~ 1.3) due to the highly suppression of mean field effect.

Together with Eq (2.13), those kinematic conditions enable the clean measurement of high momentum nucleons from SRCs and meanwhile, largely eliminate the contribution from mean field effect, such as MECs and IC.

2.2.2 Inclusive Measurement

The inclusive cross section measurement of $A(e,e')$ reaction in quasi-elastic region was firstly applied to isolate SRCs and currently is the only way to probe 3N-SRC. The cross section for $x > 1.3$ and $Q^2 > 1\ GeV^2$ is written as [29]:

$$\begin{aligned}\sigma_A(x_{bj},Q^2) &= \sum_{j=2}^{A}\frac{A}{j}a_j(A)\sigma_j(x_{bj},Q^2) \\ &= \frac{A}{2}a_2(A)\sigma_2(x_{bj},Q^2)+\frac{A}{3}a_3(A)\sigma_3(x_{bj},Q^2)+..., \qquad (2.16)\end{aligned}$$

where σ_j is the cross section for scattering from a j-nucleon correlation and $a_j(A)$ denotes the probability of finding a nucleon in this correlation. First two terms represents the contributions from 2N-SRC and 3N-SRC.

From Eq (2.3) and Eq (2.7), 2N-SRC (3N-SRC) predicts the scaling of the nucleon momentum distribution for heavy nucleus A with respect to Deuterium (^3He). In the region of $1.3 < x_{bj} < 2.0$ where 2N-SRC dominates, $a_2(A)$ can also be given by the cross section ratio:

$$a_2(A) = \frac{2}{A}\frac{\sigma_A(x_{bj}, Q^2)}{\sigma_D(x_{bj}, Q^2)}, \tag{2.17}$$

where $\sigma_D(x_{bj}, Q^2)$ is the cross section for scattering from the Deuterium target. $a_2(A)$ is identical to the one defined in Eq (2.3) and the formula indicates that at 2N-SRC region, the value of a_2 is independent of x_{bj} and Q^2, but only relates to the nuclear number. The value of the ratio on the scaling plateau directly gives the relative number of 2N-SRC pairs in the nucleus.

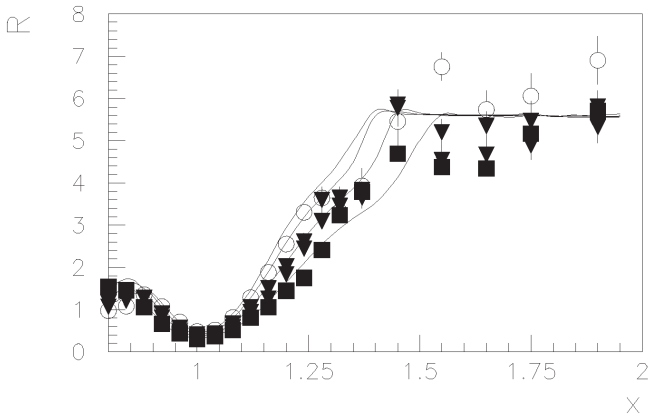

Figure 2.10: First evidence of 2N-SRC from SLAC [30]. Y-axis is the cross section ratio of ^{56}Fe to ^2H for $Q^2 = 1.2 - 2.9\ GeV^2$ and x-axis is x_{bj}. The plateau of 2N-SRC clearly is clearly showed at $x_{bj} > 1.5$ and agrees with the theoretical prediction based on the 2N-SRC model (lines).

Fig 2.10 shows the experiment results from SLAC [30], which firstly observed such a plateau using the cross section ratio of ^{56}Fe to ^2H at $x_{bj} > 1.5$ and $Q^2 =$

$1.2 - 2.9\ GeV^2$. However, the statistic were limited and the Deuterium data were taken at different kinematics, so the result was extracted with nontrivial extrapolations. Recent Jefferson Lab results from Hall-B using Large Acceptance Spectrometer (CLAS) [31] and from E02-019 data in Hall-C [32] studied the values of a_2 for various nuclei with higher statistics and better resolutions, and both results show strong agreement at the 2N-SRC region (Fig 2.11 and Fig 2.12).

Similarly, one can study 3N-SRC at $2 < x_{bj} < 3$ with the cross section ratio of the heavy nucleus to ^3He:

$$a_3(A) = K \cdot \frac{3}{A} \frac{\sigma_A(x_{bj}, Q^2)}{\sigma_{^3He}(x_{bj}, Q^2)}, \tag{2.18}$$

which is the same as the one in Eq (2.3) and denotes the number of ^3He-like 3N-SRC configuration in the nucleus. K is a kinematic constant to correct difference of the electron-proton and electron-neutron cross sections:

$$K = \frac{\sigma_{ep} + \sigma_{en}}{Z\sigma_{ep} + (A - Z)\sigma_{en}}. \tag{2.19}$$

The CLAS data for the first time measured the kinematic region of 3N-SRC and observed the plateau raises at $x_{bj} > 2.3$. The E02-019 data, however, yields a different approach in this region. From Fig 2.12, the cross section ratio of $^4He/^3He$ reaches the scaling region slightly later than the CLAS result ($x_{bj} > 2.5$). And the scaling plateau can not be conformed due to the large error bars, mainly because of the large statistic subtraction to remove the contamination from target cells. Direct interpolation of the discrepancy is impossible since two experiments ran at very different Q^2 range ($Q^2 \sim 1.6\ GeV^2$ for CLAS and $Q^2 \sim 2.7\ GeV^2$ for E02-019). It is not clear that both measurements were able to isolate the 3N-SRC contributions. The new experiment in Hall-A, E08-014, focuses on studying the scaling of 3N-SRC at $x_{bj} > 2$ with much more accuracy, and the new preliminary results will be presented in this thesis.

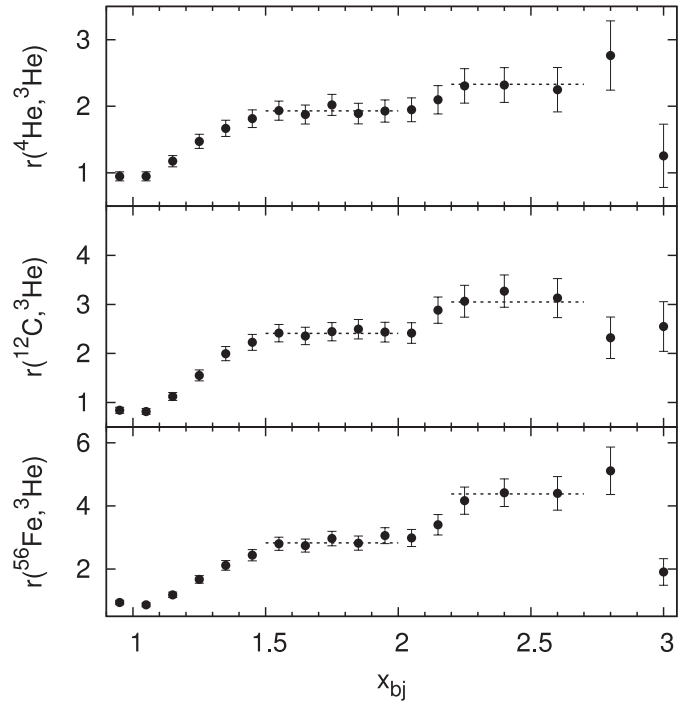

Figure 2.11: 2N-SRC and 3N-SRC results from Hall B [31].

The other important study of SRCs in inclusive measurements is the difference of two scaling variables, x_{bj} and α_i. From Eq (2.11), the LC variable α_i is approximately equal to x_{bj} at large Q^2. At low GeV^2, the approximation is not valid and the difference of the scaling behaviour in SRCs as a function of x_{bj} or α_i is required to be carefully examined. Although α_i can not be reconstructed in inclusive scattering, one can assume that in PWIA the virtual photon interacts with the nucleon in an 2N-SRC at rest. This assumption leads to a new expression of the LC variable specifically for 2N-SRC:

$$\alpha_{2N} = 2 - \frac{q_- + 2m}{2m}\frac{\sqrt{W^2 - 4m^2} + W}{W}, \tag{2.20}$$

where q_- is the initial longitudinal momentum of the struck nucleon and $W^2 =$

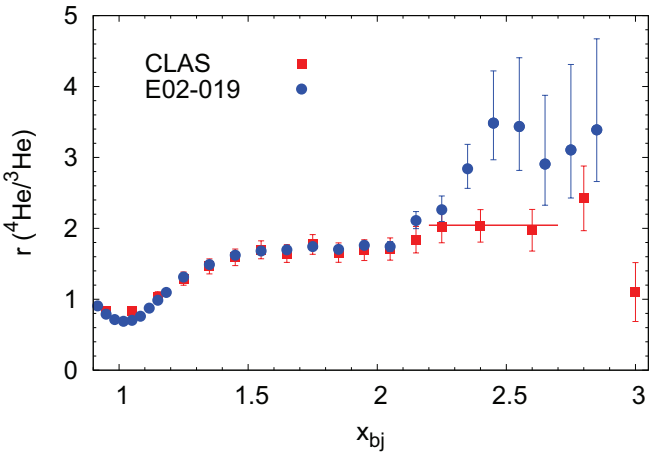

Figure 2.12: 2N-SRC and 3N-SRC results from E02-019 in Hall C [32] comparing with the result from Hall-B, where the blue dots are the E02-019 data and red dots are the CLAS data.

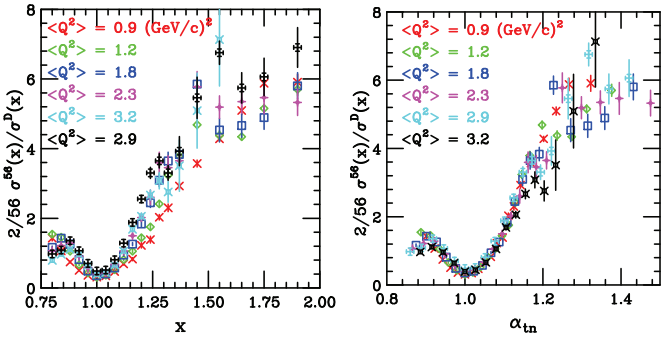

Figure 2.13: Ratio of $^{56}Fe/^2H$ as a function of x_{bj} (left) and α_{2N} (right) for different Q^2 values [30], which shows that the LC variable provides better scaling behaviour.

$4m_N^2 + 4m_N\nu - Q^2$. The analysis of SLAC data [30] reveals that α_{2N} can better isolate 2N-SRCs (Fig 2.13) and allows one to examine the transition region from 2N-SRC to 3N-SRC. A more general expression for all α_i in the inclusive measurement

can be obtained from [26]:

$$q_- \cdot \alpha_{jN} m_N + q_+ \cdot \left(M_A - \frac{M_r^2}{m_N(j - \alpha_{jN})} \right) = m_N^2, \tag{2.21}$$

where $j = 2, 3, ...$, q_+ is the initial transverse momentum of the struck nucleon and M_r is the mass of the residual system. Taking $j = 3$ can solve for α_{3N} but the exact expression depends on the value of M_r since 3N-SRC has much more complicated configuration. As discussed in previous section, 3N-SRC-I is the dominant configuration in 3N-SRC where $M_r = 2m_N$, and give:

$$\alpha_{3N} = \frac{3}{2} + \frac{1}{2}[\sqrt{(3 + b_1)^2 - b_2} - b_1] \tag{2.22}$$

where,

$$b_1 = \frac{q_+}{q_-}\frac{M_A}{m_N} - \frac{m_N}{q_-}, \qquad b_2 = 16\frac{q_+}{q_-}. \tag{2.23}$$

The value of M_r becomes higher for non-parallel configuration, such as 3N-SRC-II. Examining the scaling as a function of α_{3N} and varying the value of M_r provides a sensitive probe to the detailed structure of 3N-SRC [26].

2.2.3 Semi-Inclusive Measurements

Proton-knock-out experiments allow the direct access of the proton's initial momentum distribution through the reconstruction of the nuclear spectral function from the exclusive cross sections. In addition to measuring the scattered electron, one can map out the effect of SRCs to the high momentum tail by detecting the struck proton. Since the correlated nucleon in 2N-SRC ejected on the opposite direction is not detected, one generally treats the $A(e, e'p)$ reaction as semi-inclusive process.

To evaluate the deviation of a theoretical calculation of the momentum distribution to the experimental cross section, a normalization factor is introduced in

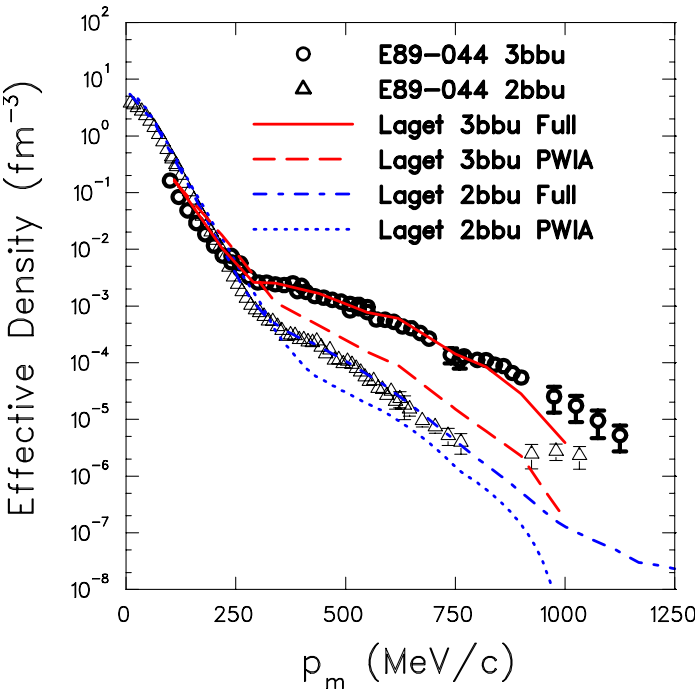

Figure 2.14: Proton Effective Momentum distribution in ^3He [33], where circles and triangles are experimental data in $^3He(e,e'p)pn$ and $^3He(e,e'p)d$, respectively. Lines are theoretical calculations from [34].

Eq (1.10) (for only one proton case) [35]:

$$\frac{d^6\sigma}{(dEd\Omega)_e(dEd\Omega)_p} = K\sigma_{ep}S(E_0,\mathbf{p_0})T_A(Q^2), \tag{2.24}$$

where K is a kinematic factor and the transparency, T_A is the probability that a nucleon will be emitted from the nucleus with other effects, such as FSI. Experiments in Hall-C [36–38] measured the values of T_A for several nuclei which were found to be higher than the predictions in IPSM. Such an enhancement is mainly due to the SRCs effect [35].

Hall-A experiments [33,39] studied the momentum distribution of ^3He target and observed that the strength greatly increases in the high momentum tail compared with the expected strength that has already included SRCs (Fig 2.14). This scenario is explained as an interference between SRCs and FSI.

2.2.4 Triple-Coincidence Measurements

An triple-coincidence experiment, $A(e, e'pN)$, performs an exclusive cross section measurement which detects the scattered electron, the struck nucleon and the spectator nucleon in 2N-SRC. Such an experiment not only can directly conforms the production of 2N-SRC, but also can study the types of the nucleon pairs involved in the correlation. This experimental techniques has been proposed in the 1960's but only been carried out with the high luminosity and high energy electron beams [40–42].

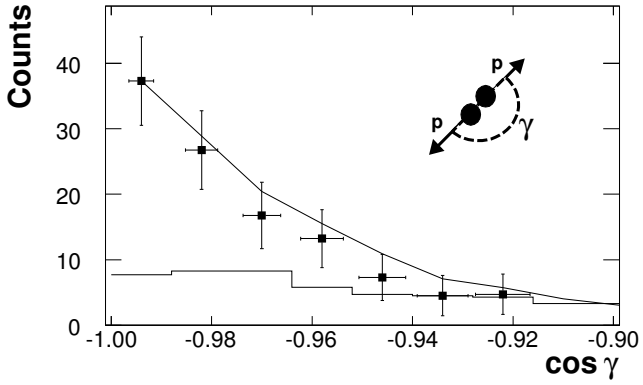

Figure 2.15: Angular correlation between nucleons in 2N-SRC, where the x-axis is the cosine of the opening angle between the struck nucleon and the spectator nucleon in the $^{12}C(e, e'pp)$ reaction [41].

A recent experiment in Hall-A, E01-015, [41, 42], has performed such a measurement using electron scattering on carbon target. In the $^{12}C(e, e'pp)$ reaction, the experiment studied the angular correlations between the struck proton and the spectator nucleons, and conformed that the correlated nucleons are back-to-back ejected from the nucleus (Fig 2.15). The ratio of pn and pp in 2N-SRC can be extracted by using the measurement of $^{12}C(e, e'pp)$ and $^{12}C(e, e'pn)$. Fig 2.16 shows that the ratio of np/pp pairs is around 18 ± 5, which conforms that the 2N-SRC is dominated by the two-body tensor interaction.

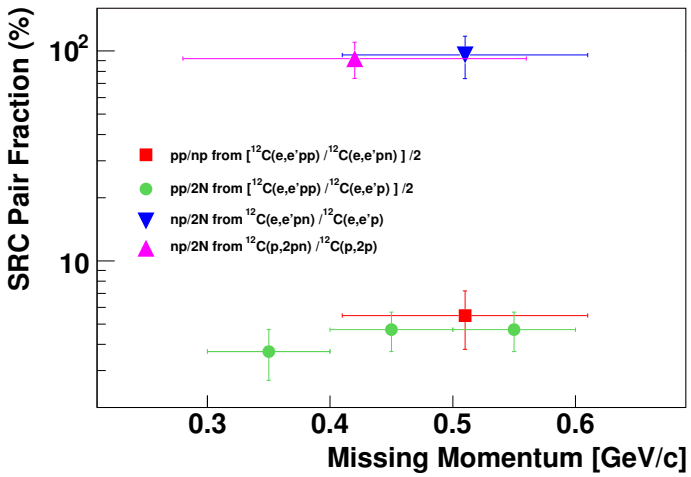

Figure 2.16: The fraction of *np* pairs to *pp* pairs in 2N-SRC in carbon from the triple-coincidence experiment in Hall-A [42].

2.2.5 Final State Interaction in SRCs

The effect of final state interaction (FSI) is proportional to $1/Q^2$. At low Q^2 the contribution of FSI is large enough to break down the y-scaling feature of quasi-elastic scattering in PWIA [43]. The study of SRCs using inclusive cross section measurement requires sufficient Q^2 values to eliminate the FSI contribution. The current results of inclusive data (i.e. in Fig 2.13) indicate no dependence of Q^2 for the scaling region of 2N-SRC, which proves that in the kinematic settings of SRCs study ($Q^2 > 1\ GeV^2$) FSI has very small contributions.

The argument above is valid since the SRCs configurations are weakly interacting with other components in the nucleus and PWIA in the inclusive measurement is still applicable. However, the contribution of FSI within the SRC may not vanish even at very large Q^2. When the electron scattering on the nucleon in SRCs, the struck nucleon stays very close to other correlated nucleons and the probability of rescattering from the residual system is large. Despite the possible large contributions, FSI is localized in the SRCs and its contribution can be removed by taking the cross section ratio. For example, the FSI contribution in the 2N-SRC pairs in heavy nuclei

should be similar to one in ^2H, and the ratio, $\sigma_A/\sigma_{^2H}$, should be able to cancel the FSI effect and only yields the clean contribution from 2N-SRC.

2.3 E08014 Experiment

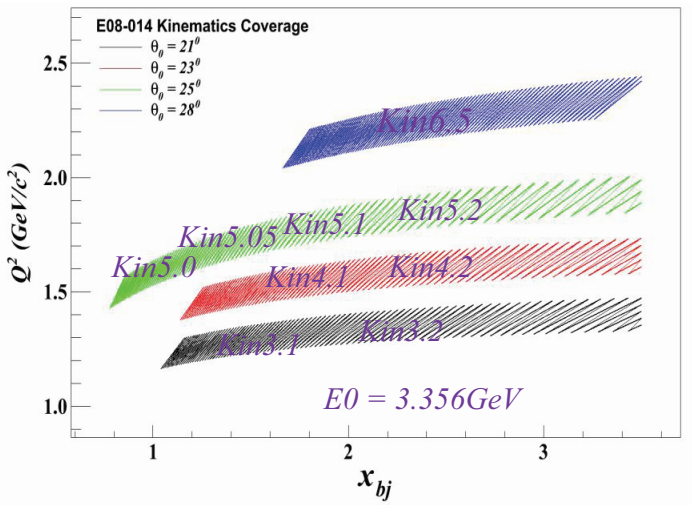

Figure 2.17: Kinematic Coverage of E08-014 experiment.

An new experiment, E08-014 [26], had been carried out in 2011 in Hall-A at Jefferson Lab, with electron beam energy of $3.356GeV$ from the continuous electron beam accelerator facility (CEBAF). Utilizing the high resolution spectrometers in their standard configurations, as shown in Fig 2.17, this experiment measured the inclusive cross section of ^2H, ^3He, ^4He, and ^{12}C at $1.1 < Q^2 < 2.5(GeV/c)^2$, which covers the range of x_{bj} from the quasi-elastic peak region to above 3.0. The absolute cross section results will be used to study the scaling function and momentum distribution at larger missing momentum, as well the effect of FSI. By taking the cross section ratio of heavy targets to ^2H or ^3He, one can examine the x_{bj} and Q^2 dependence and SRCs, and measure the values of a_2 and a_3. The relatively low Q^2 setting allows the study of α_{2N} and α_{3N} in the scaling of SRCs. The Calcium isotopes, ^{40}Ca and ^{48}Ca, were also used to study the isospin dependence of 2N- and

3N-SRC. Detailed experiment setup and data analysis will be discussed in this thesis and preliminary results will also be presented.

Bibliography

[1] D. Lacroix, Review of mean-field theory.

[2] P. Navrátil *et al.*, Phys. Rev. Lett. **87**, 172502 (2001).

[3] D. Day, private communication.

[4] R. D. Woods and D. S. Saxon, Phys. Rev. **95**, 577 (1954).

[5] N. S. Szabo and A. Ostlund, Modern quantum chemistry.

[6] L. Lapiks, Nuclear Physics A **553**, 297 (1993).

[7] J. Kelly, Adv. Nucl. Phys. **23**, 75 (1996).

[8] B. Frois and C. N. Papanicolas, Ann.Rev.Nucl.Part.Sci. **37**, 133 (1987).

[9] O. Benhar, D. Day, and I. Sick, Rev. Mod. Phys. **80**, 189 (2008).

[10] J. Arrington, Inclusive Electron Scattering From Nuclei at x¿1 and High Q2, 1998.

[11] D. Tomańek and M. A. Schluter, Phys. Rev. B **36**, 1208 (1987).

[12] J. D. Forest, Nucl. Phys. **A392**, 232 (1983).

[13] G. B. West, Physics Reports **18**, 263 (1975).

[14] C. Ciofi degli Atti, S. Liuti, and S. Simula, Phys. Rev. C **41**, R2474 (1990).

[15] S. Boffi, C. Giusti, and F. Pacati, Physics Reports **226**, 1 (1993).

[16] C. Ciofi degli Atti, D. B. Day, and S. Liuti, Phys. Rev. C **46**, 1045 (1992).

[17] O. Benhar, Phys. Rev. C **87**, 024606 (2013).

[18] C. Ciofi degli Atti and S. Simula, Phys. Rev. C **53**, 1689 (1996).

[19] J. Arrington, D. Higinbotham, G. Rosner, and M. Sargsian, Progress in Particle and Nuclear Physics **67**, 898 (2012).

[20] L. FRANKFURT, M. SARGSIAN, and M. STRIKMAN, International Journal of Modern Physics A **23**, 2991 (2008).

[21] L. Frankfurt and M. Strikman, Physics Reports **76**, 215 (1981).

[22] M. Alvioli, C. C. d. Atti, and H. Morita, Phys. Rev. C **72**, 054310 (2005).

[23] R. Subedi *et al.*, Science **320**, 1476 (2008), 0908.1514.

[24] S. C. Pieper and R. B. Wiringa, Annual Review of Nuclear and Particle Science **51**, 53 (2001).

[25] R. Schiavilla, R. B. Wiringa, S. C. Pieper, and J. Carlson, Phys. Rev. Lett. **98**, 132501 (2007).

[26] D. H. J. Arrington, D. Day and P. Solvignon, Three-nucleon short range correlations studies in inclusive scattering for $0.8 < Q^2 < 2.8(GeV/c)^2$, `http://hallaweb.jlab.org/experiment/E08-014/`, 2011.

[27] D. H. J. Arrington, D. Day and P. Solvignon, Precision measurement of the isospin dependence in the 2N and 3N short range correlation region, `http://www.jlab.org/exp_prog/proposals/11/PR12-11-112.pdf`, 2014.

[28] M. Sargsian *et al.*, Journal of Physics G: Nuclear and Particle Physics **29** (2003).

[29] L. Frankfurt and M. Strikman, Physics Reports **160**, 235 (1988).

[30] L. L. Frankfurt, M. I. Strikman, D. B. Day, and M. Sargsyan, Phys. Rev. C **48**, 2451 (1993).

[31] CLAS Collaboration, K. S. Egiyan *et al.*, Phys. Rev. Lett. **96**, 082501 (2006).

[32] N. Fomin *et al.*, Phys. Rev. Lett. **108**, 092502 (2012).

[33] Jefferson Lab Hall A Collaboration, F. Benmokhtar *et al.*, Phys. Rev. Lett. **94**, 082305 (2005).

[34] J. Laget, Physics Letters B **609**, 49 (2005).

[35] D. Higinbotham, E. Piasetzky, and S. Wood, J.Phys.Conf.Ser. **299**, 012010 (2011), 0908.0062.

[36] D. Abbott *et al.*, Phys. Rev. Lett. **80**, 5072 (1998).

[37] K. Garrow *et al.*, Phys. Rev. C **66**, 044613 (2002).

[38] E97-006 Collaboration, D. Rohe *et al.*, Phys. Rev. C **72**, 054602 (2005).

[39] Jefferson Lab Hall A Collaboration, M. M. Rvachev *et al.*, Phys. Rev. Lett. **94**, 192302 (2005).

[40] A. Tang *et al.*, **90**, 042301 (2003).

[41] Jefferson Lab Hall A Collaboration, R. Shneor *et al.*, Phys. Rev. Lett. **99**, 072501 (2007).

[42] Jefferson Lab Hall A Collaboration, R. Subedi *et al.*, Science **320**, 1476 (2008).

[43] D. Day *et al.*, Phys.Rev.Lett. **59**, 427 (1987).

[44] J. Alcorn *et al.*, Nucl. Instrum. Meth. **A522**, 294 (2004).

[45] Z. Ye, E08-014 BPM and raster alibration, 2012.

[46] P. V. J. Berthot, Nucl. Phys. News **9**, 12 (1990).

[47] O. Ravel, 1997.

[48] Jefferson lab cryogenic group, `wwwwold.jlab.org/eng/cryo`.

[49] D. Meekins, E08-014 target report, `http://hallaweb.jlab.org/experiment/E08-014/analysis/HallA_Target_Configuration_Apr2011.pdf`, 2011.

[50] R. Bock and A.Vasilescu, *The Particle Detector Brief ook* .

[51] E. Jastrzembski, 1997.

[52] Root/c++ analyzer for hall a.

[53] Root - a data analysis framework by cern, `http://root.cern.ch/drupal/`.

[54] N. Liyanage, Optics Calibration of the Hall A High Resolution Spectrometers using the new optimizer, `http://hallaweb.jlab.org/publications/Technotes/files/2002/02-012.pdf`, 2002.

[55] Hall A survey report 1343, `http://www.jlab.org/eng/survalign/documents/dthalla/A1343.pdf`, 2010.

[56] Hall A survey report A1249, `http://www.jlab.org/eng/survalign/documents/dthalla/A1239.pdf`, 2009.

[57] Hall A survey report A1239, `http://www.jlab.org/eng/survalign/documents/dthalla/A1249.pdf`, 2009.

[58] G. Jin, Measurement of the Target Single-Spin Asymmetry in Quasi-Elastic 3He, 2011.

[59] J. Huang, HRS Optics Optimizer, 2009.

[60] A. Ketikyan *et al.*, About Shower Detector Software, 1997.

[61] H. Lu *et al.*, Shower Calibration and Efficiency for E97-110, `ShowerCalibrationandEfficiencyforE97-110,http://hallaweb.jlab.org/experiment/E97-110/tech/shower_calib.ps.gz"`, 2005.

[62] E08-014 Harp scan results, 2012.

[63] P. Solvignon-Slifer, E08-014 BCM calibration report, 2012.

[64] P. Solvignon-Slifer, E08-014 BCM calibration report, 2012.

[65] Z. Ye, XEMC inclusive electron scattering cross section model, 2012.

[66] A. Duer, Single Arm Monte Carlo for Polarized 3He experiments in Hall A v.0.2, `http://hallaweb.jlab.org/publications/Technotes/files/2001/01-004.pdf`, 2002.

[67] H. Yao, Ph.D Thesis, Temple University , 2011.

[68] J. LeRose, HRS transportation functions.

[69] N. Fomin, Ph.D Thesis, University of Virginia, 2008.

[70] A. Daniel, Ph.D Thesis, Houston University, 2007.

[71] R. D. McKeown, Phys. Rev. Lett. **56**, 1452 (1986).

[72] J. S. O'Connell *et al.*, Phys. Rev. C **35**, 1063 (1987).

[73] J. Bevelacqua, FIZIKA **1**, 129 (1992).

[74] J. W. Lightbody and J. S. O'Connell, Comput. Phys. **2**, 57 (1988).

[75] K. Slifer, Ph.D Thesis, Temple University , 2003.

[76] W. Armstrong, InSane - QFS model, `http://quarks.temple.edu/~whit/code/InSANE++/html/da/dfc/group__xsections.html`.

[77] P. Bosted and V. Mamyan, Empirical Fit to electron-nucleus scattering, 2012, arXive 1203.2262.

[78] P. E. Bosted and M. E. Christy, Phys. Rev. C **77**, 065206 (2008).

[79] L. W. MO and Y. S. TSAI, Rev. Mod. Phys. **41**, 205 (1969).

[80] S. Stein *et al.*, Phys. Rev. D **12**, 1884 (1975).